論文 / 著書情報
Article / Book Information

Title	Plasma-driven sulfonation activation: Unveil a green pathway for sulfonated carbon acid catalysts
Authors	Siqi Deng, Kaixun Yao, Manabu Kodama, Katsuyuki Takahashi, Kosuke Tachibana, Junko Hieda, Oi Lun Li, Nozomi Takeuchi
Citation	Applied Surface Science, Vol. 741, , p. 167120
Pub. date	2026, 5
DOI	https://dx.doi.org/10.1016/j.apsusc.2026.167120
Creative Commons	Information is in the article.

Applied Surface Science 741 (2026) 167120

Contents lists available at ScienceDirect

Applied Surface Science

journal homepage: www.elsevier.com/locate/apsusc

Full Length Article

Plasma-driven sulfonation activation: Unveil a green pathway for sulfonated carbon acid catalysts

Siqi Deng [a,b,*], Kaixun Yao [b], Manabu Kodama [c], Katsuyuki Takahashi [d], Kosuke Tachibana [e], Junko Hieda [f], Oi Lun Li [g,h], Nozomi Takeuchi [b]

[a] Department of Electrical Engineering, Tohoku University, Japan
[b] Department of Electrical and Electronic Engineering, Institute of Science Tokyo, Japan
[c] Department of Mechanical Engineering, Institute of Science Tokyo, Japan
[d] Department of Systems Innovation Engineering, Iwate University, Iwate, Japan
[e] Department of Innovative Engineering, Oita University, Oita, Japan
[f] Graduate School of Engineering Chemical Systems Engineering, Nagoya University, Aichi, Japan
[g] School of Materials Science and Engineering, Pusan National University, Busan, South Korea
[h] Institute of Materials Technology, Pusan National University, Busan, South Korea

ARTICLE INFO

Keywords:
Plasma sulfonation mechanism
Sulfonated carbon acid catalysts
Sulfate radicals
–OSO_3H and –SO_3H functional groups

ABSTRACT

Sulfonated carbon catalysts are widely employed in acid-catalyzed biomass transformations. However, their conventional synthesis typically relies on harsh conditions. Plasma-driven sulfonation has recently emerged as a sustainable alternative that enables effective functionalization using dilute sulfuric acid with short treatment times, but the underlying reaction mechanisms remain poorly understood. Herein, we elucidate the liquid-phase reaction pathways governing plasma-assisted carbon sulfonation by combining DC plasma treatment with controlled UV and heat activation of sodium persulfate ($Na_2S_2O_8$) solutions as reference systems. Comparative analysis reveals that sulfate radicals ($\bullet SO_4^-$), generated via plasma–liquid interactions or persulfate activation, play a key role in sulfur incorporation, leading to the formation of sulfonic (–SO_3H) and sulfate ester (–OSO_3H) groups alongside oxygen-containing functionalities on carbon surfaces. This work establishes a mechanistic framework for plasma-driven carbon sulfonation and provides fundamental insights into plasma–liquid chemistry, supporting the rational design of sustainable sulfonated carbon catalysts under mild conditions.

1. Introduction

Sulfonated carbon materials have attracted considerable attention as solid Brønsted acid catalysts owing to their high acid density, structural tunability, and broad applicability in biomass-related transformations and other acid-catalyzed reactions. Early efforts to introduce –SO_3H onto carbon materials can be traced to the patent by Rivin et al. [1], who developed a sulfonation method using fuming sulfuric acid. Later, Hara et al. demonstrated that SO_3H-modified carbons as versatile solid Brønsted acid catalysts, and successfully applied them in a biomass-transformation process [2–4]. After that, extensive research has focused on synthesizing high-performance sulfonated carbon catalysts from natural organic precursors and employing them in a wide range of acid-catalyzed transformations, including the hydrolysis of polysaccharides, esterification of acetic acid and ethanol, biodiesel production via triglyceride transesterification, hydration, and dehydration [5–8]. Although several variations of the method have been developed over the past decade, fuming sulfuric acid is required to obtain a sulfonated carbon catalyst with high acidic site density [5], posing environmental and safety concerns. These limitations highlight the need for an environmentally friendly approach for fabricating high-performance sulfonated carbon catalysts. Li et al. developed a novel carbon sulfonation technique using plasma discharge inside [9,10] as well as above dilute sulfuric acid [11,12]. However, the underlying reaction mechanism of plasma sulfonation remains insufficiently understood, which hinders rational optimization and further enhancement of sulfonation efficiency.

Low-temperature plasma has emerged as an effective and environmentally benign medium for modifying carbon materials [13,14]. For example, O_2 plasma treatment has been shown to enhance the surface

* Corresponding author at: Department of Electrical Engineering, Tohoku University, Japan.
E-mail address: deng@tohoku.ac.jp (S. Deng).

https://doi.org/10.1016/j.apsusc.2026.167120
Received 13 February 2026; Received in revised form 18 April 2026; Accepted 2 May 2026
Available online 4 May 2026

chemistry of carbon and improves the shear strength of composite interfaces [15,16]. Beyond gas-phase plasmas, gas–liquid interfacial plasma has attracted increasing attention as a versatile approach for carbon functionalization, primarily because hydroxyl radicals (•OH) can be generated in large quantities through plasma–liquid interaction [17–19]. Compare to atmospheric-pressure plasma jets with humidity gas typically produce ~ 10^{18} m^{-3} [20,21], continuous DC positive discharge with a liquid electrode can reach •OH densities with 10^{21} m^{-3} [22]. Which indicate that liquid-electrode plasmas are efficient way to produce reactive oxygen species for carbon modification. Moreover, when different solvents or ionic species are introduced into the liquid phase, plasma–liquid interactions can generate additional reactive radicals beyond •OH, enabling the incorporation of diverse functional groups onto carbon surfaces [23].

In our previous study, the formation of SO_2, condensed H_2O, and H_2SO_4 aerosols during pulsed plasma discharge in dilute sulfuric acid was confirmed [24], suggesting that H_2SO_4 undergoes partial thermal decomposition, generating H_2O, O_2, and SO_2, while oxidizing species produced in the gas phase react with these sulfur-containing intermediates to form sulfur-containing functional groups on carbon surface. Sulfur-containing radicals are expected to form in this plasma discharge. Among them, the $\bullet SO_4^-$ has attracted particular attention owing to its high reactivity. Jiang et al. reported that $\bullet SO_4^-$ can be produced through reactions between •OH and HSO_4^- or H_2SO_4 [25].

$$\bullet OH + HSO_4^- \rightarrow \bullet SO_4^- + H_2O \quad (1)$$

$$\bullet OH + H_2SO_4 \rightarrow \bullet SO_4^- + H_3O^+ \quad (2)$$

The standard electrode potential of $\bullet SO_4^-$ is ≈2.5–3.1 V [26], comparable to •OH (2.8 V) [27]. Because of this strong oxidizing ability, $\bullet SO_4^-$ obtained through alkaline activation [28], UV irradiation [29,30], heat [29], and metal oxide [31] on persulfate solutions, is widely used in wastewater and waste gas treatment [32–34]. $\bullet SO_4^-$ enable the degradation of pollutants such as azo dye Acid Orange 7 within 45 min at 80 °C [29].

Owing of its high reactivity and short lifetime, direct detection of $\bullet SO_4^-$ in H_2SO_4 solution is extremely challenging, particularly in plasma discharge. To date, there have been no reports providing direct experimental evidence for $\bullet SO_4^-$ formation during plasma discharge. Consequently, the role of $\bullet SO_4^-$ in plasma-driven sulfonation must be evaluated indirectly through reaction outcomes and carefully designed comparative experiments. Therefore, in this study, we first compare sulfonation efficiency and catalytic performance treated under positive and negative DC plasma discharges with varying treatment times. Subsequently, UV and heat activation of 0.1 ~ 0.5 mol/L sodium persulfate ($Na_2S_2O_8$) solution are employed as controlled reference systems to selectively generate $\bullet SO_4^-$ and evaluate their specific contribution to carbon sulfonation.

2. Experimental setup

2.1. Materials

Multiwalled carbon nanotubes (MWCNTs, JEIO 6A; diameter: 5 ~ 7 nm; length; 50 ~ 150 um) were used as the carbon precursor. Ultrapure water was prepared using an ultrapure water generation unit (Merck Millipore Direct-Q UV; resistance value: ~18MΩ • cm). H_2SO_4 solutions (1.0 M) were prepared from concentrated H_2SO_4 (98 wt%, Wako), and $Na_2S_2O_8$ (PS) solutions were prepared by dissolving $Na_2S_2O_8$ powder (Kanto Chemical) in ultrapure water. Cellulose (Sigma, powder, 20 μm) and cellobiose (Sigma, powder, ≥99.0%) were used for hydrolysis.

2.2. Carbon-treatment setups

As illustrated in Fig. 1, 300 mg of MWCNTs were dispersed in 50 mL 1 M H_2SO_4 solution and subjected to 2 polarity direct-current (DC) plasma treatment, as described in detail in the Supporting Information. For comparison experiments to the plasma treatment, 300 mg of MWCNTs were mixed with 50 mL of $Na_2S_2O_8$ solution at three different concentrations and placed in an Erlenmeyer flask. Two persulfate activation methods were employed: 1. Thermal activation, in which the suspension was heated and maintained at 80 °C using a water bath (AS

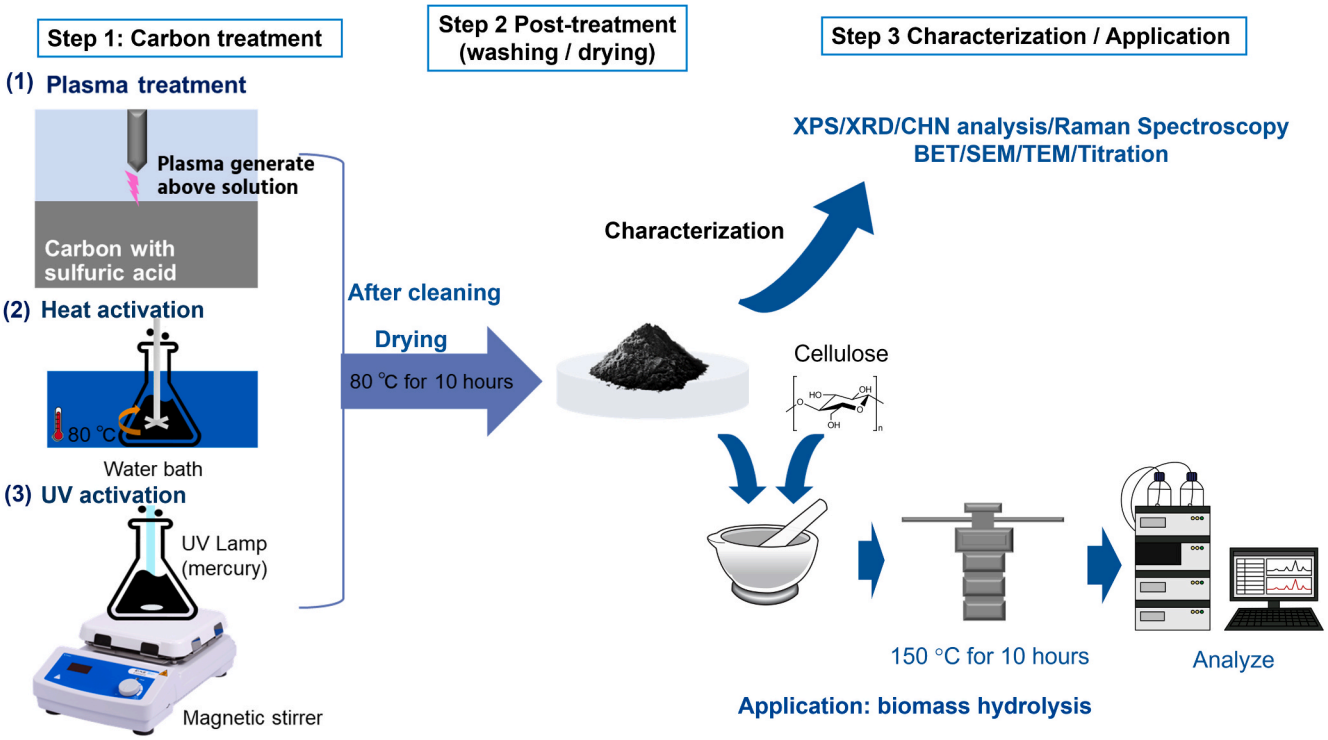

Fig. 1. Schematic illustration of the carbon sulfonation process.

ONE HWA-50D); 2. UV activation, where the suspension was irradiated using a mercury lamp (HAMAMATSU L6212-05, see Fig. S2) while being magnetically stirred at 500 rpm (Yamato Mag-Mixer MD200). The hydrothermal method was used as a control group, in which MWCNTs were treated with concentrated sulfuric acid (18 M) in an oven (ISUZU VTEC) at 150 °C for 10 h. After treatment, the samples were separated by vacuum filtration using a hydrophilic polytetrafluoroethylene (PTFE) membrane filter (Merck, 0.45 μm pore size; JHWP04700), thoroughly washed with ultrapure water, and dried in an oven at 80 °C for 10 h.

2.3. Carbon characterization

2.3.1. X-ray photoelectron spectroscopy (XPS)

Ex situ XPS was performed using a PHI 5000 VersaProbe III. In this experiment, a monochromatic Al Kα (1486.6 eV) X-ray source was used to generate photoelectrons. Survey scans were performed with a resolution of 0.4 eV and a pass energy of 112 eV, while element-specific scans were conducted with a resolution of 0.2 eV and a pass energy of 27 eV. The results were analyzed using MultiPak, and the fitting curve was obtained using a mixed Lorentzian–Gaussian function.

2.3.2. CHNS elemental analysis

The densities of sulfur-containing functional groups (–SO_3H&–OSO_3H) and other oxygen-containing functional group densities were estimated from CHNS elemental analysis in combination with XPS results. The sulfur density was measured using a HSU-20 (Yanako) + ICS-1100 (Thermo Fisher Scientific) with a combustion cube temperature of 950℃. The oxygen density was determined using a Vario Macro Cube (Elementar) with a combustion cube temperature of 1150℃.

2.3.3. Raman spectroscopy

The defects on the carbon surface were analyzed using Raman spectroscopy (JASCO, NRS-4100, 532 nm diode laser) with an integration time of 60 s. The resolution and laser intensity were set as 1 cm^{-1} and 0.1 mW, respectively.

2.3.4. Brunauer–Emmett–Teller (BET) method

The specific surface area (S_{BET}) was calculated using the Brunauer–Emmett–Teller (BET) equation. A Microtrac MRB BELSORP mini X was used to analyze the specific surface area pore size distribution. The pore size distribution was calculated from the N_2 adsorption isotherm using the Barrett (Joyner) Halenda method. Before the BET measurement, a 100 mg carbon sample was heated under vacuum to 120 °C for 24 h.

2.3.5. X-ray diffraction (XRD) measurements

The crystal structures of the CNTs and cellulose were obtained using XRD (MiniFlex, Rigaku). The diffractometer was equipped with a Cu X-ray source with a voltage and current of 40 kV and 15 mA, respectively. The detector was a D/teX Ultra2, and the step width was 0.01°.

2.3.6. Scanning electron microscopy (SEM) & transmission electron microscopy (TEM)

TEM images were captured using a JEM-2010F field-emission electron microscope (JEOL) at an accelerating voltage of 200 kV. SEM and energy-dispersive X-ray spectroscopy (EDS) mapping images were obtained using a TM4000 (Hitachi) + QUANTAX 75–60 (Bruker). The acceleration voltage was 15.0 keV, and the magnification is x2000.

2.4. . Catalytic performance determination

The catalytic performance of the treated carbon was evaluated in cellulose and cellobiose hydrolysis reactions. For cellulose hydrolysis, 100 mg of cellulose, 100 mg of catalyst, and 10 mL of ultrapure water were mixed by agate mortar and loaded into a 25 mL Teflon-lined stainless-steel autoclave (Yuanyu; 25 mL). Prior to hydrolysis, cellulose was ball-milled at 650 rpm for 5 5 days using an AV-2 ball mill (Asahi-rika) with porcelain jars (Φ105 mm; Nitto Kagaku Co.). The autoclave was then heated at 423 K for 24 h in an oven (VTEC-75, Isuzu Cap). Cellobiose hydrolysis experiments were conducted under identical conditions using 100 mg of cellobiose as the substrate. After reaction, the mixture was cooled to room temperature and filtered through a PTFE membrane (Merck; 0.1 μm). The concentrations of glucose and other soluble products were analyzed using a Shimadzu high-pressure liquid chromatography (HPLC) system equipped with an RID-20A detector and a Shodex Sugar KS-802 column, and data were processed using Shimadzu LabSolutions software. Byproducts such as levulinic acid and formic acid were quantified using ion chromatography (Metrohm 883 Basic IC Plus) equipped with a Shodex SI-50 4E column. The total concentration of water-soluble products was determined using a TOC analyzer (Shimadzu TOC-L CSH). Glucose yield and cellulose conversion were calculated using the following equations:

$$Glucose\ yield(\%) = \frac{C_{glucose} \times V / M_{glucose}}{m_{cellulose} / M_{cellulose}} \times 100$$

$$Cellulose\ conversion(\%) = \frac{C_C \times V}{R \times m_{cellulose}} \times 100$$

Cellulose conversion is defined as the fraction of initial cellulose converted.

Glucose yield is defined as the fraction of initial cellulose converted to glucose.

Glucose selectivity is defined as the fraction of converted cellulose forming glucose. Where $C_{glucose}$ is the glucose concentration determined by HPLC (g L^{-1}), V is the solution volume (0.01 L), $M_{glucose}$ and $M_{cellulose}$ are molar mass of glucose (180 g·mol^{-1}) and molar mass of glucose unit in cellulose (162 g mol^{-1}), C_C is the carbon concentration measured by TOC (g·L^{-1}). R is the fraction of carbon in cellulose, and $m_{cellulose}$ is the initial mass of cellulose(g).

3. Results and discussion

3.1. Modification by DC plasma discharge with dilute sulfuric acid

During DC plasma discharge, the solution temperature varied depending on the polarity of the discharge (Table S2), primarily owing to the characteristics of the glow discharge. Under positive discharge (also referred to as liquid cathode discharge), the cathode sheath near the liquid surface causes a significant voltage-drop, heating the solution. By contrast, under negative discharge (liquid anode discharge), the majority of the thermal energy is deposited at the metal electrode rather than in the liquid phase [35]. The optical emission spectrum obtained during the negative discharge indicates the presence of black body radiation from the tip of the metal electrode (Fig. S1), which corresponds to the intense bright emission observed experimentally and can be attributed to electrode heating. The plasma–liquid contact area during positive discharge is approximately 12.57 mm^2 and during negative discharge is near 1.40 mm^2 (Fig. 2). Besides the intense emission from the electrode, a purple glow was observed in both discharge modes, which is attributed to the nitrogen second positive system [36]. In addition, emission from hydroxyl radicals was detected at approximately 309 nm [37]. Notably, mist formation depended on the discharge polarity [38]. In positive discharge, visible mist formation occurred after approximately 10 min of plasma treatment, whereas under negative discharge, mist formation was significantly delayed and appeared only after around 40 min.

To confirm the plasma treatment results, SEM images with EDX mapping were obtained (Fig. S3). After plasma treatment, compared with the original CNTs, in addition to oxygen and carbon, a proportional amount of sulfur was present in the materials. Fig. 3 summarizes the

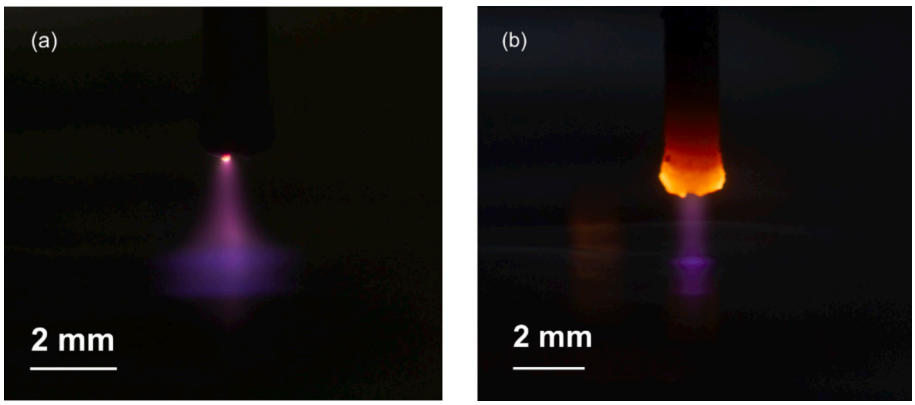

Fig. 2. Photographs of (a) positive and (b) negative DC plasma discharge above 1 M H_2SO_4 solution (exposure time: 1/80 s; ISO: 125).

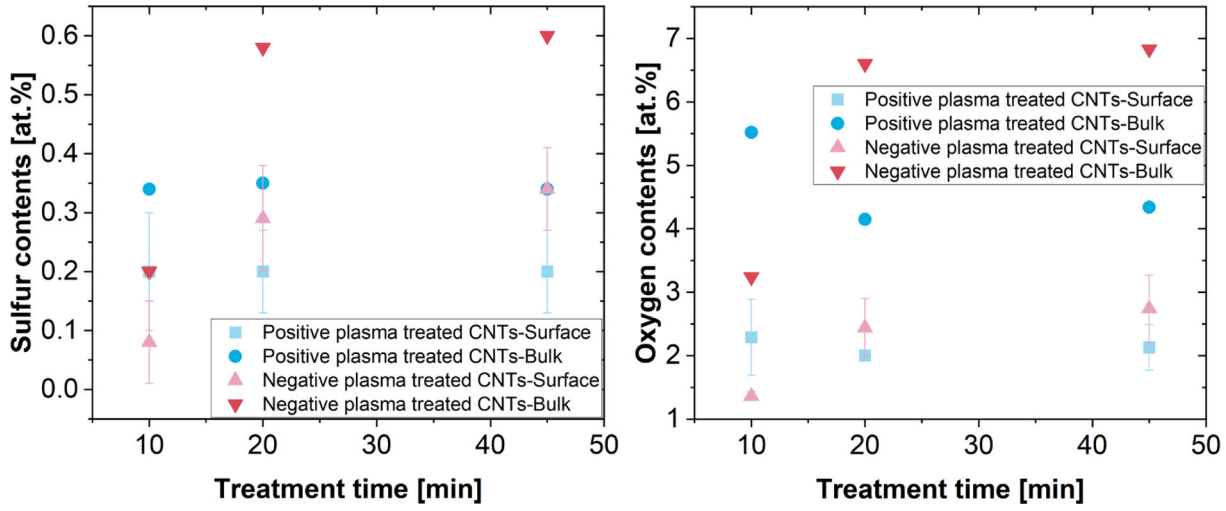

Fig. 3. Variation of (left) sulfur content and (right) oxygen content in CNTs treated by positive and negative DC plasma discharge as a function of treatment time. Surface elemental compositions were determined by XPS, while bulk elemental compositions were obtained by CHN elemental analysis.

evolution of sulfur and oxygen contents determined by CHN (bulk) analyses, and curve fitting of each XPS survey spectrum (Fig. S4). After positive discharge treatment, the surface sulfur concentration reaches a plateau after approximately 10 min of treatment, whereas a continuous increase is observed under negative discharge. In contrast, the evolution of oxygen content differs from that of sulfur, particularly for positive discharge. Both XPS and CHN analysis indicate a decrease in oxygen content with extended treatment time, suggests that oxygen-containing groups formed at early stages may undergo surface reorganization or conversion into sulfur-containing functionalities rather than continuous accumulation.

In addition, XPS was used to determine the chemical status of the elements and each density in the material. As shown in Fig. 4(a, b, c), the main peak in the C 1s spectra is attributed to C=C (284.3–284.6 eV) and C−C (284.7–285.0 eV) bonds in graphitic carbon [39]. Oxygen-containing C 1s peaks also appear in these spectra. The hydroxyl groups (C−OH), the carbonyl group (C=O), and the carboxylic acid groups (O=C−OH) are located at 286.4 ± 0.2 eV, 287.9 ± 0.2 eV and 289.6 ± 0.2 eV, respectively. Excluding the oxygen-containing C 1s peaks, the π–π bond is located at 290.7 ± 0.2 eV [40–42].

The fitting results summarized in Fig. 4(a, b, c) and Table 1, indicate that both positive and negative plasma treatments increase the surface density of oxygen containing functional groups (OFGs), although their absolute contributions differ depending on the discharge polarity. To provide independent confirmation of oxygen functionalization, O 1s spectra were additionally analyzed (Fig. S5). In agreement with the C 1s fitting results, O 1s spectra show a progressive increase in OFGs related components with increasing plasma treatment time, supporting that plasma treatment effectively introduces OFGs on the CNT surface. The formation of –OH, C=O, and –COOH groups can be consistent with oxidation induced by •OH through reaction (3)–(5), which is a well-established pathway in plasma–liquid interaction systems [19,43]:

$$\bullet OH + M \rightarrow M{-}OH \quad (3)$$

$$\bullet OH + M{-}OH \rightarrow M{-}COOH \quad (4)$$

$$\bullet OH + M{-}OH \rightarrow M{-}C{=}O + H_2O \quad (5)$$

Here, M denotes a reactive carbon site on the CNT surface, including defect sites, edge sites, or unsaturated carbon atoms.

In the S 2p XPS spectra [Fig. 4(d, e)], the peaks at 168.3 and 169.5 eV are assigned to S $2p_{3/2}$ and S $2p_{1/2}$ of $–SO_3H$, while the peaks at 169.3 and 170.5 eV correspond to $–OSO_3H$. Plasma treated CNTs reveal the coexistence of $–SO_3H$ and $–OSO_3H$, with an approximate $–SO_3H/–OSO_3H$ ratio of 80/20 (Table 1). In contrast, sulfur content on the sulfonated carbon material obtained after the hydrothermal process is only attributed to the formation of $–SO_3H$ (as illustrated in Fig. S6(a)), indicating that the mechanism of plasma sulfonation is different from the traditional sulfonation process. In addition to the $–SO_3H$ and $–OSO_3H$ groups, thiol-type sulfur species (–SH) were also detected in the plasma-treated CNT sample, based on the low-binding-energy component in the S 2p XPS spectrum (Fig. S7). The –SH group is mainly due to reduction by the

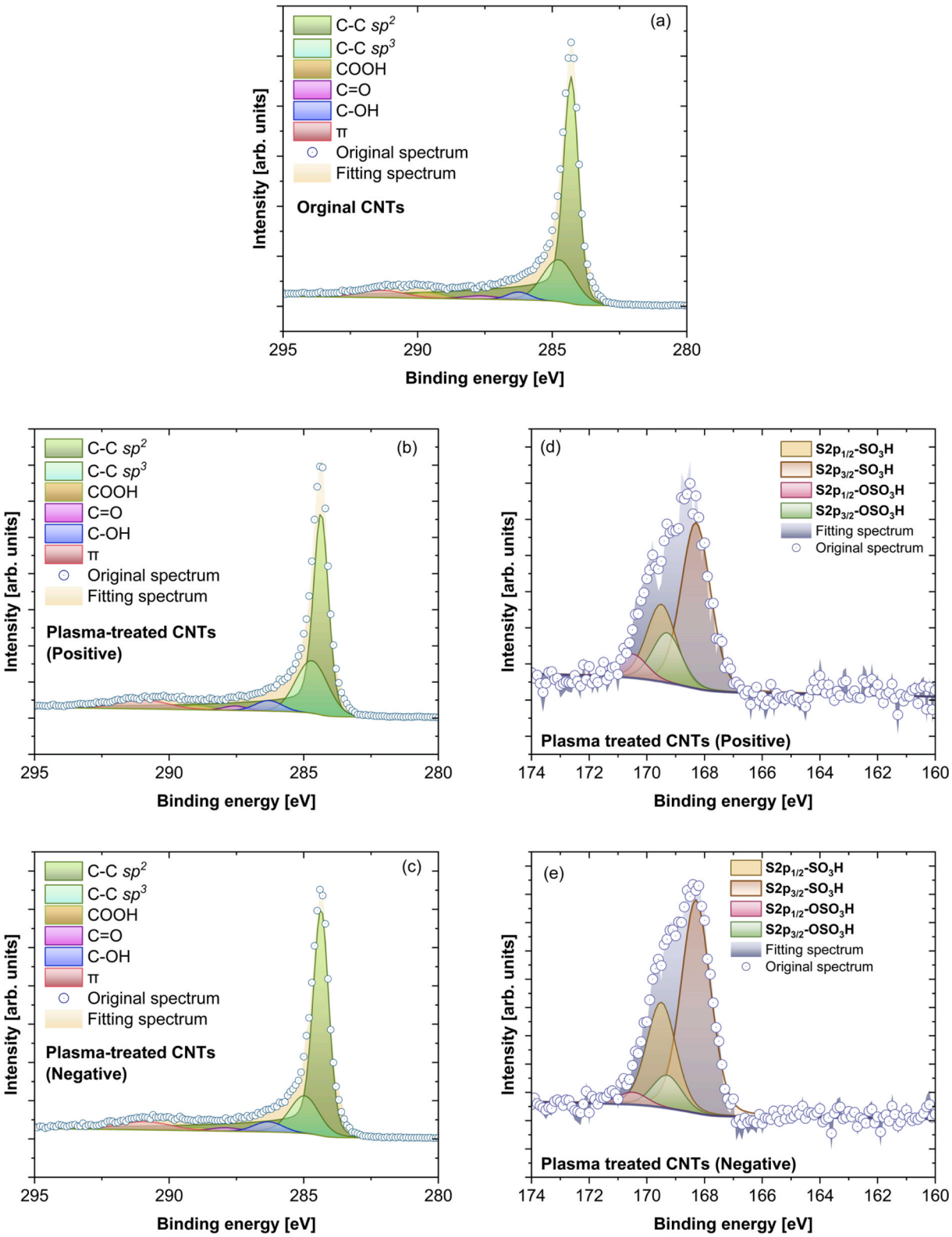

Fig. 4. (a–c) C 1 s XPS spectra and (d, e) S 2p XPS spectra of original CNTs and CNTs after 45 min of DC positive and negative discharge plasma treatment. During curve fitting, for C 1 s fitting, the main graphitic sp^2 carbon component was described using an asymmetric line shape characteristic of aromatic/graphitic carbon. To ensure consistency, the asymmetry of the sp^2 component was kept constant for all CNT-based samples; for S 2p fitting, the full width at half maximum (FWHM) of each S 2p component was fixed at 1.2 eV, and the area ratio of S $2p_{3/2}$ to S $2p_{1/2}$ was constrained to 2:1 [50].

reducing agents in the plasma discharge, such as electrons and hydrogen radicals, and carbothermal reduction of the –SO_3H group [5]. To further support the S 2p analysis, S 2s spectra were also examined (Fig. S8), with most signals observed around 232 eV. Notably, the S 2s peak of CNTs treated under positive discharge is located at a slightly higher binding energy (~233 eV) than that observed for negative discharge. This shift is consistent with the S 2p fitting results, indicating a relatively higher –OSO_3H /–SO_3H ratio in the positive plasma-treated CNTs.

In addition to XPS and CHNS analyses, the total acid density was measured using an acid–base titration method, as described in the Supporting Information (Section S2). It should be noted that acid–base titration quantifies the total number of proton-dissociable sites, whereas XPS and CHNS analyses provide information on elemental composition and the relative abundance of specific functional groups. The variation of total acid density for plasma-treated CNTs is shown in Fig. S9. The results indicate that the acid density increases with treatment time, which is consistent with the trends observed in XPS and CHNS analyses. In addition, samples treated under negative discharge exhibit relatively higher acid densities, suggesting enhanced formation of surface functional groups under these conditions.

In addition, FTIR analysis was performed to provide complementary information on the surface functional groups, as described in the Supporting Information (Section S3). O–H stretching at approximately 3400 cm^{-1} which is related to –OH, C=O stretching which is related to C=O or –COOH groups at 1701 cm^{-1}, C=C stretching at 1602 cm^{-1} [44,45], and CH stretching at 2920 cm^{-1} [46], and O–H bending mode at 1400 cm^{-1} [47]. For the treated CNTs, additional bands were observed in the range of 1000–1200 cm^{-1}, which can be attributed to S=O/S–O stretching vibrations associated with –SO_3H and –OSO_3H [46,48,49], which considered as supportive evidence for the presence of –SO_3H and –OSO_3H (Fig. S10).

3.2. Modification by sulfate radicals

To elucidate the sulfonation mechanism involved in plasma treatment, carbon materials were modified using $\bullet SO_4^-$ generated via UV and heat activation of $Na_2S_2O_8$ solutions, both of which are well-established routes for $\bullet SO_4^-$ production in liquid phase. These two activation methods were therefore employed as controlled reference systems to isolate the role of $\bullet SO_4^-$ in carbon sulfonation.

XPS and CHN elemental analyses were also carried out to determine the densities of the sulfur- and oxygen-containing functional groups. As shown in Fig. 5, heat activation treatment led to a pronounced decrease in sulfur contents with increasing treatment time, whereas the reduction in sulfur contents induced by UV activation was comparatively moderate. For both activation methods, a comparable maximum sulfur content on the order of ~1 at.% was typically achieved within the first 10 min, indicating rapid initial incorporation of sulfur-containing species. In

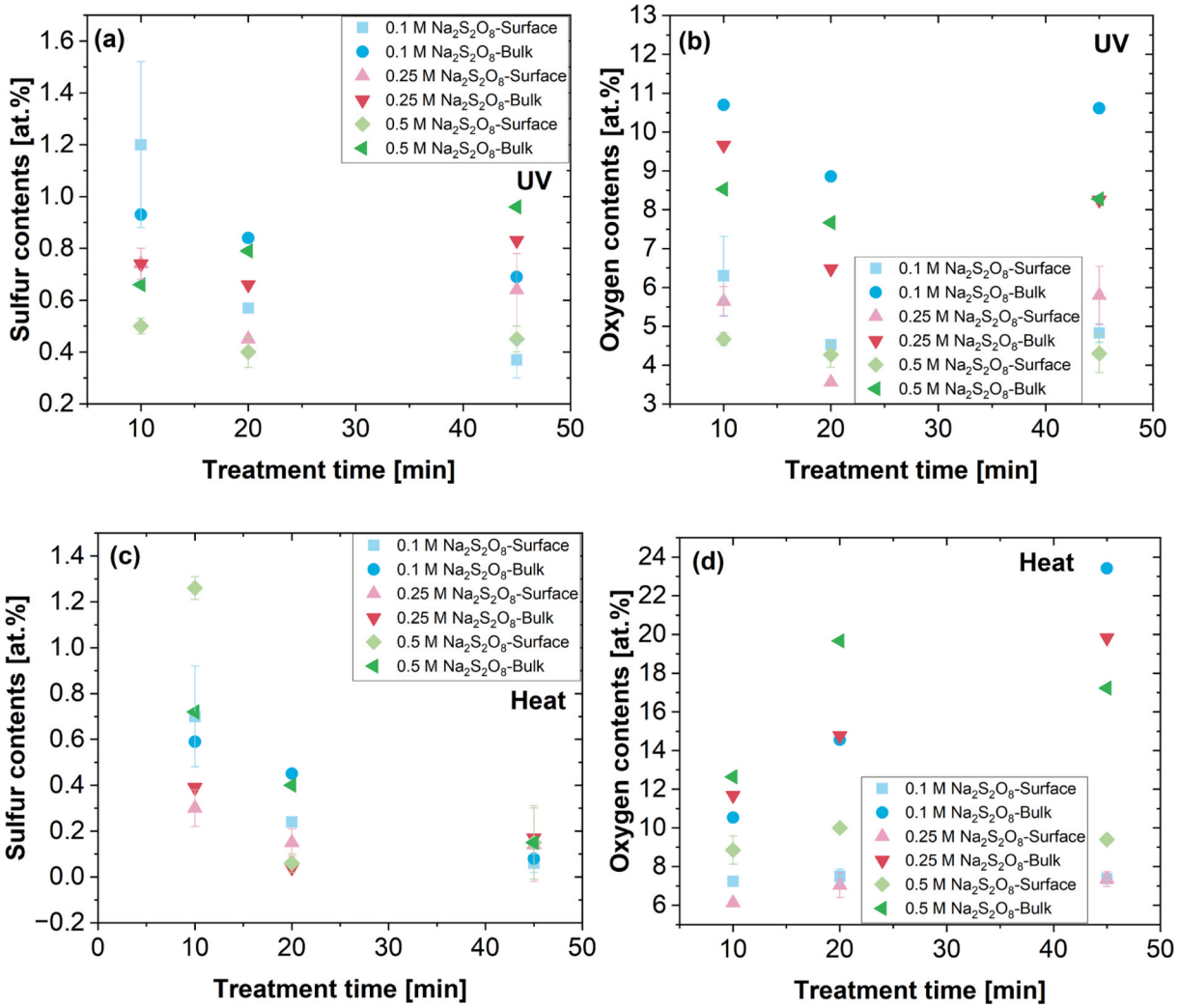

Fig. 5. (a, c) Variation in sulfur content and (b, d) oxygen content in CNTs treated by $Na_2S_2O_8$-UV activation and −heat activation treatment as a function of treatment time and $Na_2S_2O_8$ solution concentration. Surface elemental compositions were determined by XPS, while bulk elemental compositions were obtained by CHN elemental analysis.

contrast, the evolution of oxygen content exhibited distinct trends for the two activation methods. During heat activation, the oxygen contents increased monotonically with treatment time, the bulk oxygen contents reaching a maximum value of nearly 24 at.%, suggesting extensive oxidation of the CNTs. By comparison, UV activation treatment resulted in a U-shaped variation in oxygen contents, reflecting a dynamic balance between OFGs formation and subsequent decomposition or rearrangement processes.

As shown in Fig. S9, the total acid density of the carbon material treated by UV activation increased up to 20 min of treatment and then became nearly saturated, whereas the acid density of the carbon material treated with heat activation continued to increase noticeably, even up to 45 min of treatment. It should be noted that the increase in total acid density observed during heat activation does not necessarily correspond to an increase in $-SO_3H$. Instead, this increase mainly reflects the formation of additional OFGs, as also indicated by XPS analysis. This discrepancy indicates that, despite the gradual loss of sulfur-containing groups under prolonged heat activation, the accumulation of weakly acidic OFGs, also strongly contribute to the acidity of the material. Under heat activation, the oxidation process is substantially more intense than under UV activation, leading to extensive incorporation of oxygen functionalities. As a result, the removal of sulfur-containing groups does not offset the increase in total acidity, which is dominated by the growing population of oxygen-derived acidic sites.

The C 1s and S 2p XPS spectra of CNTs treated by UV and heat activation are presented in Fig. 6, from which the evolution of surface functional groups was quantified. As summarized in Table 1, the relative contributions of oxygen-containing groups to the C 1s spectra increased with treatment time for both activation methods. In particular, heat-activated CNTs exhibited a higher fraction of –COOH groups on the carbon surface, indicating more extensive surface oxidation. The corresponding S 2p fitting results are summarized in Table 1. With increasing treatment time, the ratio of $-SO_3H$ to $-OSO_3H$ groups increased for both activation methods. Notably, after 45 min of heat activation, the $-OSO_3H$ component was almost completely eliminated, suggesting preferential removal or transformation of $-OSO_3H$ under prolonged treatment.

Overall, the combined trends in elemental composition and acid density indicate that $\bullet SO_4^-$-driven sulfonation is accompanied by concurrent oxidation and surface restructuring processes, whose relative contributions depend sensitively on the activation mode and treatment duration.

3.3. Carbon characterization results

The TEM images in Fig. 7 and Fig. S11 show the structural features of the CNTs. As indicated in the manufacturer's specifications, the CNTs have inner and outer diameters of approximately 3.8 ± 0.4 nm and 7.5

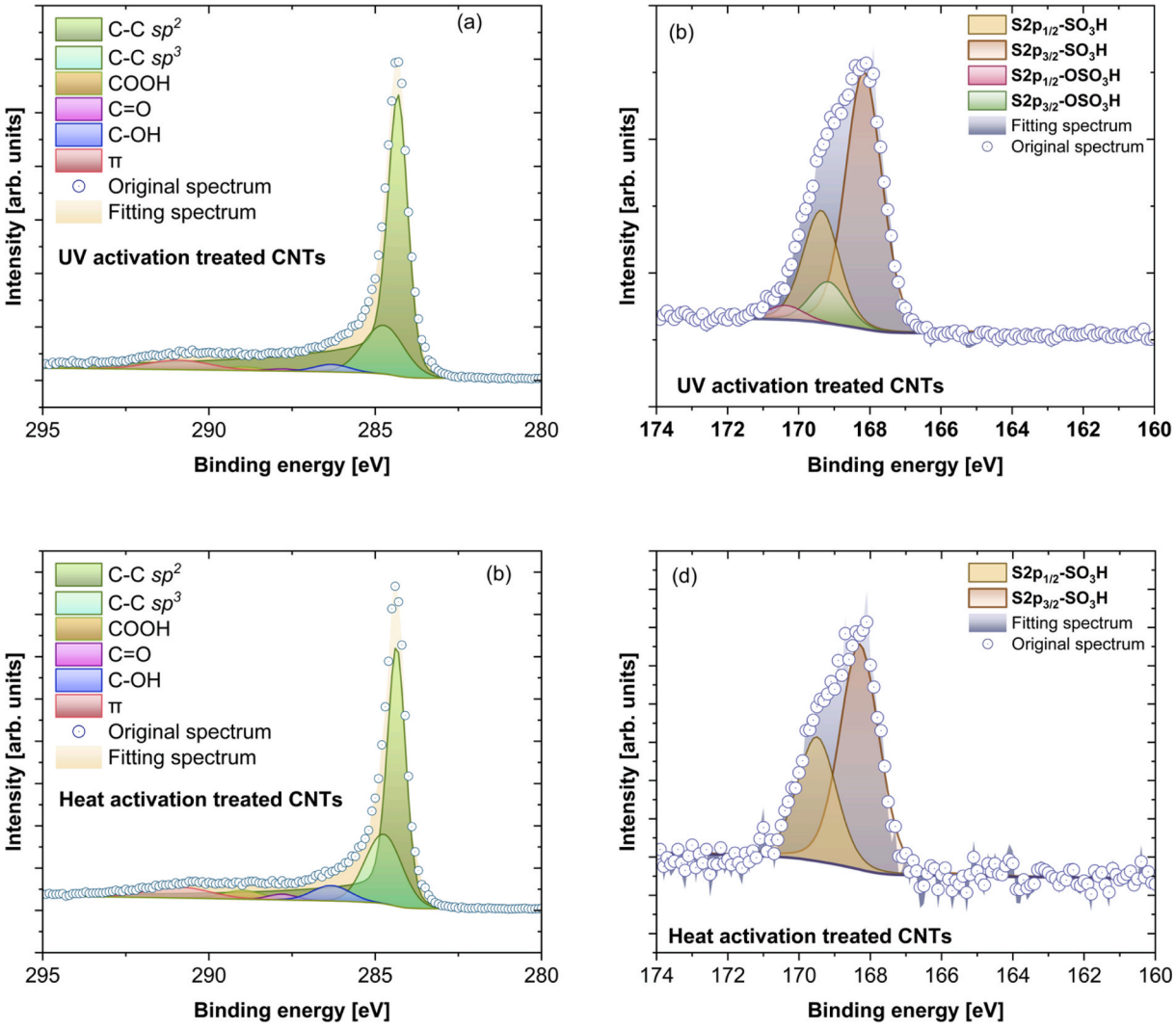

Fig. 6. (a, b) C 1s and (c, d) S2p XPS spectra of CNTs after 45 min of $Na_2S_2O_8$-UV and −heat activation in 0.25 M $Na_2S_2O_8$ solution. During curve fitting, the full width at half maximum (FWHM) of each S 2p component was fixed at 1.2 eV, and the area ratio of S $2p_{3/2}$ to S $2p_{1/2}$ was constrained to 2:1 [50].

Table 1
Specific surface area and surface chemical composition of CNTs before and after 45 min positive/negative DC plasma treatment, 45 min UV 0.25 M $Na_2S_2O_8$ activation treatment, and 45 min heat 0.25 M $Na_2S_2O_8$ activation treatment, as determined by BET and XPS analyses. 3 kinds of oxygen-containing functional groups were quantified from C 1 s deconvolution, while sulfur species were identified from S 2p fitting.

Sample	Surface area ($m^2\ g^{-1}$)	O contributions to C 1s spectra (at.%)*			Area percentage (%) of peaks contributing to S 2p*,#		
		COOH	C=O	C-OH	$-SO_3H$	$-OSO_3H$	–SH
Original CNTs	519	0.86	1.45	2.39	0	0	0
Positive discharge, 10 min	436	1.22	1.12	4.20	83.58	16.42	0
Positive discharge, 20 min	435	1.07	1.52	5.01	89.83	10.17	0
Positive discharge, 45 min	383	1.99	1.37	3.85	76.79	23.21	0
Negative discharge, 10 min	495	0.90	1.23	3.83	84.50	15.50	0
Negative discharge, 20 min	467	1.14	1.61	3.51	77.42	22.58	5.53
Negative discharge, 45 min	455	2.14	1.65	3.93	82.90	17.10	0
UV activation, 10 min	n.d.	1.81	2.11	4.39	76.71	23.29	0
UV activation, 20 min	n.d.	1.41	1.90	4.52	84.09	15.91	0
UV activation, 45 min	434	2.15	1.43	4.26	82.50	17.50	0
Heat activation, 10 min	n.d.	1.26	1.53	3.89	82.28	17.72	0
Heat activation, 20 min	n.d.	2.44	1.48	4.50	89.80	10.20	0
Heat-activation, 45 min	475	2.77	1.39	4.19	100.00	0.00	0
Hydrothermal sulfonated 10 h	340	0.94	2.54	5.29	100.00	0.00	0.00

n.d. = not determined.
* Curve fitting in this experiment was performed using a Gaussian/Lorentzian ratio of 80/20 and a Shirley baseline.
# Based on the CHNS sulfur content and the XPS-derived $-SO_3H/-OSO_3H$ ratio, the densities of $-SO_3H$ and $-OSO_3H$ groups are estimated to be approximately 0.22 and 0.07 mmol g^{-1} for CNTs treated under positive discharge for 45 min, and approximately 0.41 and 0.09 mmol g^{-1} for CNTs treated under negative discharge for 45 min, respectively.

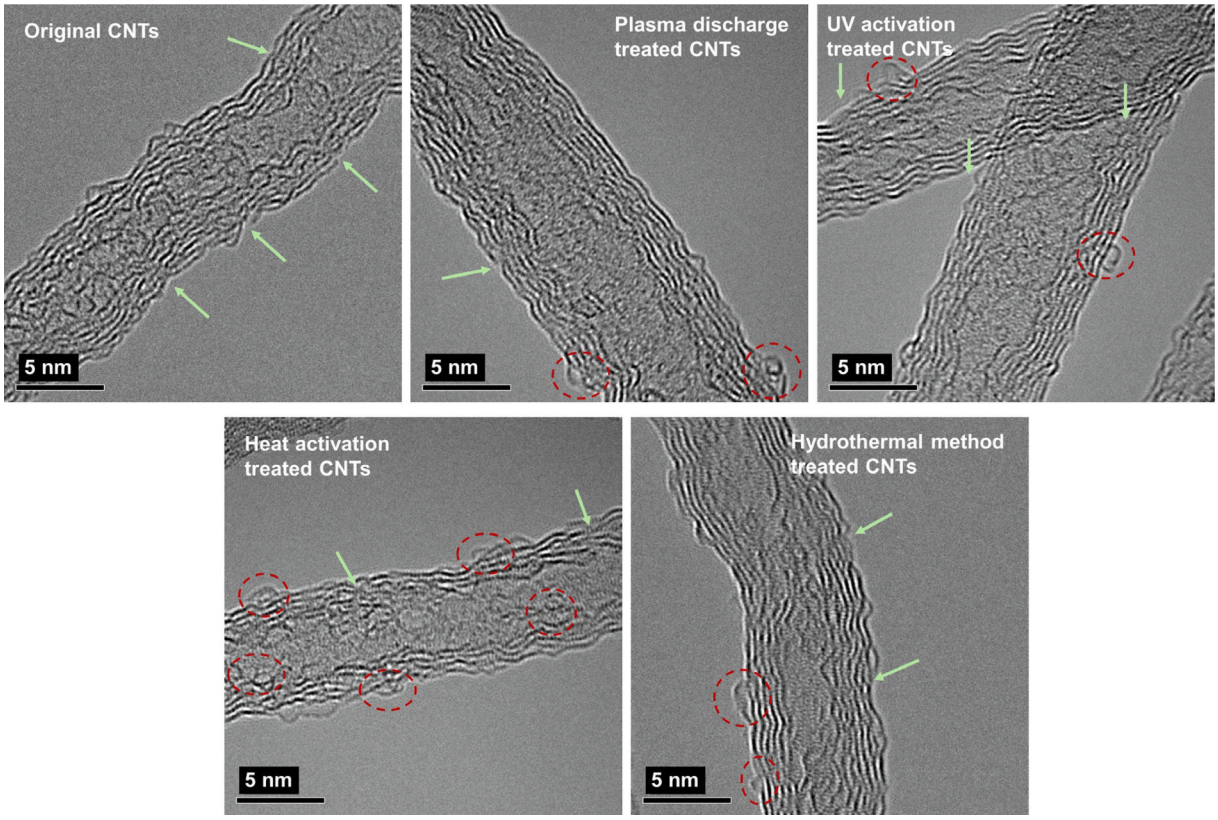

Fig. 7. TEM images of original CNTs and treated CNTs. Green arrows indicate intrinsic defects or wrinkled regions, while red dashed circles highlight localized surface reconstruction or disorder induced by different treatments.

± 0.8 nm, respectively, with 3–7 layers (Fig. 7). The presence of intrinsic defect sites on the original CNT walls makes them suitable for subsequent modifications. After plasma treatment, heat activation, and hydrothermal treatment, wrinkles appeared on the CNT surfaces (Fig. S11) [51].

After plasma treatment, the specific surface area decreased for both positive and negative discharges, with a more pronounced reduction observed for the positive discharge (Table 1). This decrease is primarily attributed to changes in the mesoscopic structural features rather than the formation or collapse of micropores. Plasma treatment slightly reduces the pore volume contribution in the 10–100 nm range (Fig. S13), which is commonly associated with inter-bundle voids and aggregated CNT networks. Surface functionalization and plasma-induced restructuring are therefore likely to promote CNT bundling and/or partial blockage of mesoporous pathways, resulting in a reduced accessible

surface area [52,53]. In addition, the higher solution temperature observed during positive discharge further facilitates surface group rearrangement and CNT aggregation. In contrast, negative discharge involves a much smaller plasma–liquid contact area, leading to a less pronounced reduction in accessible surface area despite continued sulfur incorporation at longer treatment times. After the activation treatments, the specific surface area was reduced in both cases. However, the extent of surface area reduction was smaller than that observed for CNTs treated by positive DC plasma (Table 1). Additionally, the diameter distribution of the CNTs remained consistent (Fig. S12), indicating no significant changes in diameter after other treatment.

To obtain more information on the carbon structure, Raman spectroscopy was employed to characterize the structural disorder in CNTs [Fig. 8(a)]. Raman spectra exhibit the characteristic D, G, and G' bands. D band appears when the hexagonal sp2 network has sufficient defects [54,55]. While the G band is a characteristic feature of all sp^2-carbon materials. The intensity ratio of the disorder-induced D band to the G band (I_D/I_G) is widely used as a qualitative indicator of defect density in CNTs, with higher values reflecting a greater degree of structural disorder [54]. Following positive plasma discharge treatment, a decrease in the I_D/I_G ratio was observed, indicating an apparent reduction in structural disorder. A similar trend was observed for heat-activated and hydrothermally treated CNTs. This defect reduction is primarily attributed to the relatively high solution temperatures during the experiments. Increasing the solution temperature promoted the rearrangement or removal of unstable groups, resulting in a more uniform and less defective structure. For example, residual oxygen-containing groups may migrate to form more stable configurations.

XRD analysis was conducted to evaluate the effects of various treatments on the carbon structure [56]. Fig. 8(b) presents the XRD patterns of the original and treated CNTs. The peak corresponds to the (002) reflection, which is characteristic of stacked graphene sheets, confirming the multiwalled structure of the CNTs [57]. The retention of sharpness in the (002) peak after each treatment indicates that the graphitic structure remained intact. It is well-documented that a reduction in the crystallinity of CNTs leads to broader XRD peaks and a shift of the (002) reflection toward lower angles owing to changes in interlayer spacing [56]. As shown in Table S3, most treatments, except for plasma treatment, intensified the (002) reflection and reduced the FWHM [58]. Specifically, $Na_2S_2O_8$ activation and hydrothermal treatment effectively removed amorphous carbon and residual catalyst particles, leading to a decrease in the FWHM of the (002) peak and improved crystallinity, while plasma discharge induces mild lattice perturbations due to energetic electrons and ion bombardment. Despite this, all CNT samples exhibited peaks corresponding to the (100) reflection, signifying hexagonal plane alignment and structural regularity [59]. Additionally, peaks of the (004) and (110) reflections further confirm the retention of crystallinity across all the samples.

The seemingly contrasting trends observed in Raman and XRD analyses arise from the different length scales probed by the two techniques. Raman spectroscopy is predominantly sensitive to the surface and outermost graphene layers [60], where plasma-induced heating facilitates defect healing and surface ordering. In contrast, XRD reflects the average structural order of the entire CNT, where plasma exposure can introduce subtle stacking disorder without compromising the overall graphitic structure [61]. Together, these results demonstrate that plasma treatment preserves the multiwalled architecture of CNTs while inducing controlled, surface-localized functionalization accompanied by minor bulk structural perturbations.

3.4. Sulfonation mechanism

3.4.1. Carbon sulfonation by $\bullet SO_4$

The formation and reduction of sulfur-containing functional groups during activation treatments can be attributed to carbon modification caused by the interaction with $\bullet SO_4^-$ radicals in this experiment. Specifically, $\bullet SO_4^-$can be generated through UV activation [62] and heat activation via reaction (6):

$$S_2O_8^{2-} \rightarrow 2\bullet SO_4^- \quad (6)$$

[63,64].

The oxygen atom in the $\bullet SO_4^-$ is highly reactive and can interact with carbon defect sites through oxidative pathways, leading to the formation of sulfur-containing surface functionalities, as described in reaction (7). (The benzene ring can serve as a representative model for each carbon unit in the CNTs.).

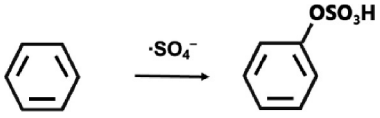

(7)

[65]

The variation in solution pH during treatment is shown in Fig. S14. Both UV activation and heat activation reduce the pH over time, decreasing to 1.5 and 1.0, respectively. This pH reduction can be explained by two key reactions: the production of •OH from $\bullet SO_4^-$ and

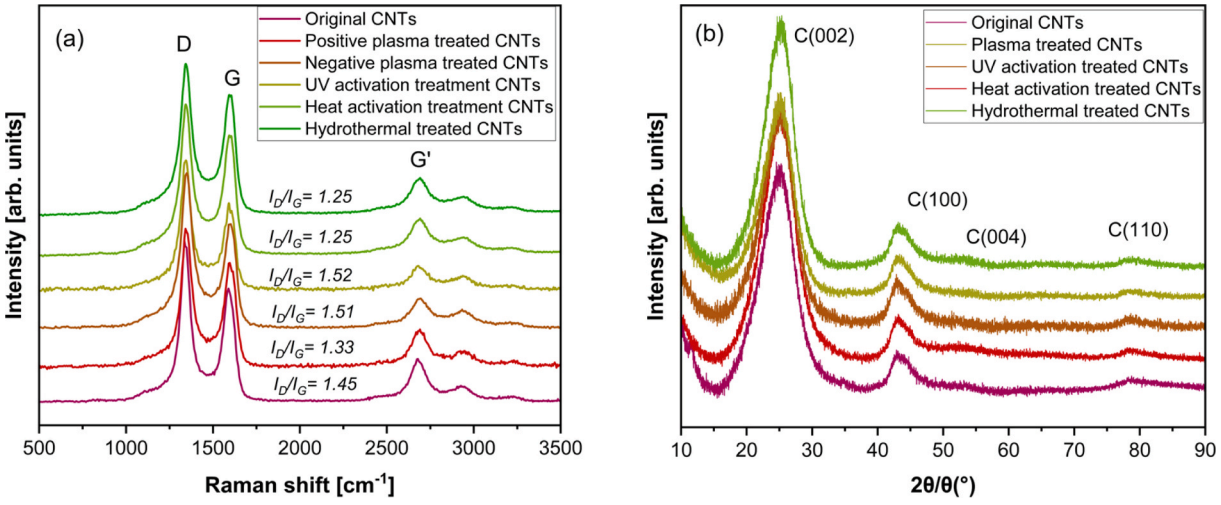

Fig. 8. (a) Raman spectra of original CNTs and treated CNTs, the D, G, and G′ bands are located at 1350 cm^{-1}, 1580 cm^{-1} and ~2700 cm^{-1}; (b) XRD patterns of original CNTs and treated CNTs, the characteristic reflections of graphitic carbon, including C (002), C (100), and C (004) are labeled, the XRD spectra contained peaks at 2θ = 25.5°, 43.0°± 0.1°, 53.8°± 0.1° and 78.5° ± 0.2°, corresponding to the (002), (100), (004) and (110) reflections, respectively.

the removal of $–OSO_3H$ groups from the CNT surface. Hydroxyl radicals were generated via the following reaction:

$$\bullet SO_4^- + H_2O \rightarrow SO_4^{2-} + \bullet OH + H^+ \quad (8)$$

[63,64].

The $–OSO_3H$ group is removed to form the C=O group and HSO_4^-, which also lowers the solution pH [66]:

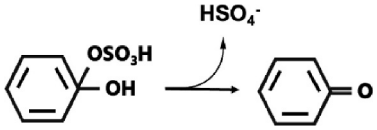

(9)

The formation of $–SO_3H$ by $\bullet SO_4^-$ remain underexplored. Two acid-catalyzed mechanisms have been proposed for the consumption of peroxydisulfate under acidic conditions (reactions (11), (12), and (13)): one mechanism produces SO_3, O_2, and H_2SO_5, while the other generates $\bullet SO_4^-$. Therefore, the production of $\bullet SO_4^-$may be reduced under strongly acidic conditions relative to neutral or alkaline systems, [67] but remains kinetically relevant under plasma-assisted conditions.

$$S_2O_8^{2-} + H^+ \rightarrow HS_2O_8^- \rightarrow HSO_4^- + SO_4 \quad (10)$$

$$\mathbf{SO_4 + H_2O \rightarrow H_2SO_5} \text{ (strongly acidic conditions)} \quad (11)$$

$$\mathbf{SO_4 \rightarrow SO_3 + 1/2O_2} \text{ (weakly acidic conditions)} \quad (12)$$

$$\mathbf{S_2O_8^{2-} + H^+ \rightarrow HS_2O_8^- \rightarrow \bullet SO_4^- + HSO_4^-} \quad (13)$$

$\bullet SO_4^-$ not only oxidize carbon but also react with SO_3 preferentially react at carbon defect sites to form $–SO_3H$.

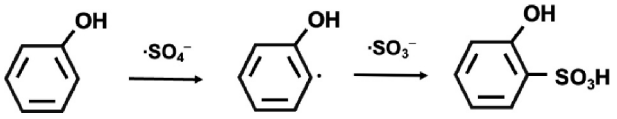

(14)

Because the sulfonation reaction is reversible [68], $–SO_3H$ can also be removed under acidic conditions. At prolonged treatment times, as suggested by the experimentally observed sulfur-content saturation, the acidic environment facilitates the removal of the $–SO_3H$, as described in reaction (15).

$$\mathbf{M–SO_3H + H^+ \rightarrow M–H + H^+ + SO_3} \quad (15)$$

The SO_3 produced in reaction (15) dissolves in solution, further reducing the solution pH.

It should be noted that plasma-assisted sulfonation under strongly acidic conditions involves a highly complex reaction environment. In addition to the competing reactions affecting $\bullet SO_4^-$ generation and the acid-catalyzed desulfonation pathways discussed above, other side reactions may also occur. These may include further oxidation or fragmentation of sulfur-containing intermediates, radical–radical recombination, transient formation of peroxysulfur species, and secondary reactions between carbon-centered radicals and oxygenated sulfur species.

3.4.2. *Carbon sulfonation by in plasma treatment*

To elucidate the sulfonation mechanism involved in plasma treatment, controlled reference experiments were conducted using UV and heat activation of $Na_2S_2O_8$ solutions, both of which are well-established routes for generating $\bullet SO_4^-$ in the liquid phase. These reference systems do not aim to reproduce the full complexity of plasma chemistry, but rather to isolate and benchmark the specific contribution of $\bullet SO_4^-$ to carbon sulfonation under acidic conditions.

XPS and CHN analyses show that sulfur incorporation occurs rapidly during the initial stage of both UV and heat activation, reaching a maximum sulfur content within the first 10 min. With prolonged heat activation, however, the sulfur content decreases markedly, while the oxygen content increases monotonically. In contrast, UV activation results in a more moderate sulfur loss accompanied by a non-monotonic, U-shaped evolution of oxygen content. These distinct trends indicate that sulfur-containing functionalities formed at early stages are progressively destabilized under strongly acidic and thermally activated conditions, whereas oxygen-containing groups continue to accumulate. The evolution of sulfur speciation further supports this interpretation. S2p fitting results show that the $–SO_3H/–OSO_3H$ ratio increases with treatment time for both activation methods, with $–OSO_3H$ eliminated after prolonged heat activation. This behavior is consistent with the preferential remove of $–OSO_3H$, as described by the pathway in reaction (9), resulting in a relative enrichment of the chemically more stable $–SO_3H$ groups. Acid–base titration measurements further clarify the apparent discrepancy between sulfur content and total acidity. Even as sulfur-containing groups decrease under prolonged heat activation, the continuous accumulation of weakly acidic oxygen-containing functionalities, such as –COOH and –OH groups, leads to a net increase in total acid density. This explains the sustained rise in acidity observed during heat activation despite declining sulfur content.

The two activation methods differ in the spatial characteristics of $\bullet SO_4^-$ generation. During heat activation, thermal decomposition of $S_2O_8^{2-}$ occurs throughout the bulk solution, providing a spatially extended reservoir of $\bullet SO_4^-$, although sulfonation remains a heterogeneous process limited to the carbon surface. By contrast, UV activation generates $\bullet SO_4^-$ predominantly within the irradiated region adjacent to the lamp surface, leading to a more localized radical generation profile. Despite these differences, both reference systems enable systematic evaluation of $\bullet SO_4^-$-driven surface functionalization. Due to resembling the localized radical generation characteristic of plasma–liquid interactions, UV activation here use to provide a mechanistic benchmark for interpreting plasma-assisted sulfonation.

During plasma treatment, •OH are generated predominantly in the gas phase near the plasma–liquid interface and subsequently diffuse toward the liquid surface. Owing to the high concentration of HSO_4^- ions in H_2SO_4 solution and the fast reaction kinetics, •OH radicals entering the liquid phase are rapidly converted into $\bullet SO_4^-$ through reaction (1). The formation rate of $\bullet SO_4^-$ is estimated approximately 4.17×10^{-7} mol/s (see Supporting Information for the detailed calculation), which is still lower than that obtained in the UV-activation reference system (5.71×10^{-6} mol/s). It should be emphasized that the formation rate of $\bullet SO_4^-$ is not directly proportional to the rate of sulfur-containing functional group formation on carbon surfaces. In plasma treatment, additional effects—such as energetic electron bombardment, surface excitation, and defect activation—can significantly enhance the reactivity of carbon surfaces, thereby facilitating sulfur incorporation even at comparatively lower $\bullet SO_4^-$ fluxes.

Because the density of sulfur-containing functional groups decreases at prolonged treatment times, the quantitative analysis was limited to the initial 10 min period, where sulfur incorporation is dominated by formation rather than removal processes. Under these conditions, UV activation of a 0.1 M $Na_2S_2O_8$ solution produces approximately 3.4×10^{-3} mol/L $\bullet SO_4^-$ in 10 min. This results in the formation of sulfur-containing functional groups, specifically $–SO_3H$ and $–OSO_3H$, with an average sulfur-containing group density of 0.9 at.%, corresponding to approximately 0.75 mmol of sulfur-containing functionalities. By comparison, after 10 min of positive discharge treatment, the average sulfur-containing group density reached 0.35 at.%, corresponding to the formation of approximately 0.25 mmol of sulfur-containing functional groups. Owing to the localized reaction zone and limited plasma–liquid contact area in plasma treatment, a direct quantitative comparison between the contributions of $\bullet SO_4^-$ generated during plasma discharge and those produced during UV activation remains challenging. Nevertheless, these results suggest that increasing the plasma–liquid contact area or employing plasma reactors with enhanced •OH production could further improve sulfonation efficiency.

Notably, although the sulfonation effect of positive discharge tended to saturate rapidly, negative discharge treatment resulted in a higher

sulfur-containing group density after 45 min. This behavior cannot be explained solely by $\bullet SO_4^-$ formation. Negative discharge is known to generate a higher electron flux but a lower •OH flux compared with positive discharge. For example, Yue et al. reported an •OH flux of approximately 2×10^{19} m^{-2} s^{-1} at a negative discharge current of 8 mA [69]. Based on this value, the formation rate of $\bullet SO_4^-$ under negative discharge conditions is estimated to be only $\approx 4.17 \times 10^{-10}$ mol s^{-1}, which is insufficient to account for the experimentally observed sulfur incorporation. The enhanced sulfonation under negative polarity suggests the involvement of additional plasma-induced processes, such as electron-driven surface activation, defect-assisted sulfur capture, or reactions involving reduced sulfur species generated in the plasma environment. These pathways likely operate in parallel with $\bullet SO_4^-$-mediated reactions and become more pronounced under negative discharge conditions.

Owing to the extremely short lifetime and high reactivity of sulfur-centered radicals under acidic conditions, direct identification of all elementary steps remains experimentally challenging. Therefore, the mechanistic framework proposed here focuses on the dominant reaction pathways supported by comparative experiments and quantitative trends. A schematic overview of the proposed plasma-driven sulfonation pathways is presented in Scheme 1.

3.5. Catalytic performance of CNTs treated by plasma discharge treatment and $\bullet SO_4^-$ modification

The performances of the synthesized catalysts were evaluated in cellulose and cellobiose hydrolysis reactions. The XRD pattern of ball-milled cellulose (Fig. S15) confirms that the crystalline structure of cellulose was effectively disrupted prior to hydrolysis, ensuring sufficient accessibility of glycosidic bonds. The yields of soluble products obtained from cellulose hydrolysis are summarized in Fig. 9. For all treated CNT catalysts, prolonged carbon treatment generally led to higher total product yields, reflecting the increased density of acidic surface functional groups. In the case of plasma-treated CNTs, the evolution of product yield with treatment time closely follows the variation in surface functional group density discussed in Section 3.1, indicating that surface acidity plays a dominant role in promoting cellulose depolymerization. The enhanced catalytic performance observed for heat-activated CNTs with treatment time is therefore attributed to a synergistic effect of residual sulfur-containing acid sites and oxygen-containing surface functionalities. OFGs may contribute to cellulose hydrolysis by improving hydrophilicity, adsorption, and interfacial proton transfer [70].

Glucose selectivity, an important metric for evaluating catalyst performance in biomass conversion, is shown in Fig. S16. For plasma-treated CNTs, glucose selectivity ranged from approximately 60–75% and exhibited a moderate dependence on discharge polarity and treatment time. The relatively low glucose selectivity observed for the 10 min negative discharge-treated CNTs can be attributed to insufficient acid site density, resulting in incomplete conversion of cellobiose intermediates. In contrast, extended positive discharge treatment led to a slight decrease in glucose selectivity, consistent with the partial loss of surface functional groups at longer treatment times. Comparatively, UV-activation treated and plasma-treated CNTs generally exhibited lower glucose selectivity than heat-activation treated CNTs. Cellulose hydrolysis catalyzed by UV-activated and plasma-treated CNTs produced larger amounts of byproducts such as 5-hydroxymethylfurfural (HMF), levulinic acid, formic acid, and other reduced sugars. These products arise primarily from secondary dehydration and fragmentation reactions of glucose. In contrast, hydrolysis using heat-activated CNTs favored the accumulation of cellobiose and residual lignocellulosic fragments, indicating milder secondary reactions.

This behavior can be rationalized by the relative abundance of strong Brønsted acid sites. Hara et al. reported that the turnover frequency (TOF) of the strongly acidic $–SO_3H$ groups in a graphene-based solid acid was about 20-fold greater than those of conventional solid acids (e.g., Amberlyst-15) and almost reached that of H_2SO_4 [71]. Accordingly, CNTs with higher $–SO_3H$/other OFGs ratios promote not only cellulose hydrolysis but also subsequent glucose dehydration, leading to reduced glucose selectivity. In contrast, heat-activation treated CNTs, which possess a higher proportion of weaker acidic oxygen-containing groups, favor selective glucose formation while suppressing excessive secondary reactions.

Compared with cellulose hydrolysis, cellobiose hydrolysis using the treated carbon catalysts resulted in markedly higher glucose yields and conversion efficiencies (Fig. 10). This improvement can be attributed to the soluble nature of cellobiose, which enables more effective contact between the catalyst surface and the substrate in the aqueous phase. Enhanced mass transfer and interfacial accessibility facilitate the cleavage of the β-1,4-glycosidic bond linking the two glucose units. Using CNTs treated by positive DC plasma discharge, cellobiose

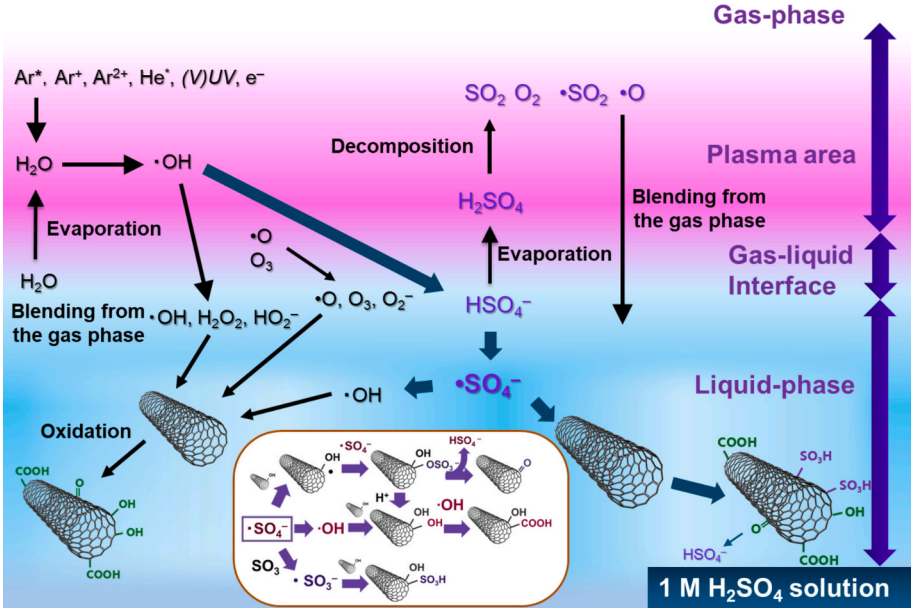

Scheme 1. Proposed mechanism of plasma-driven carbon sulfonation.

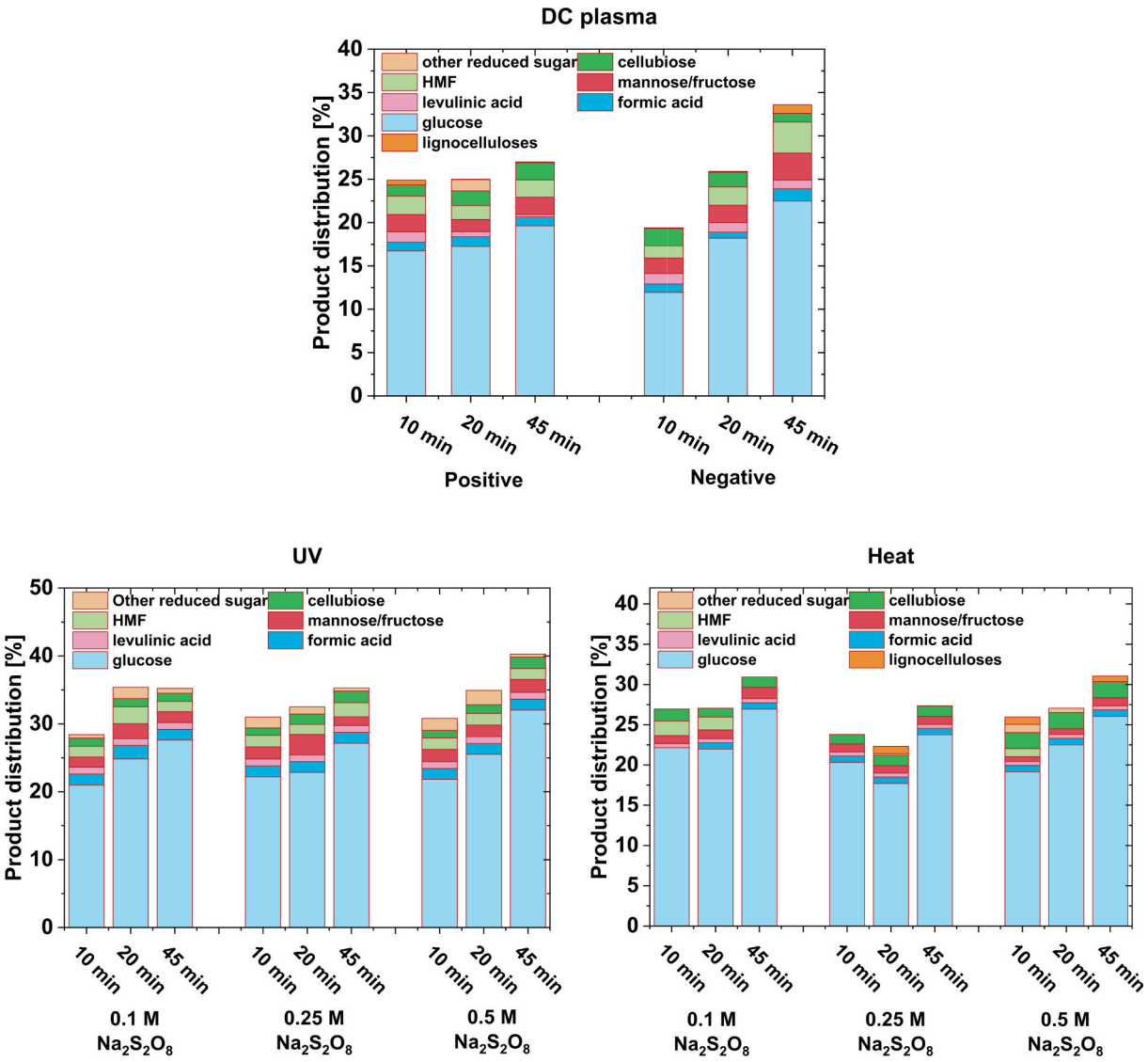

Fig. 9. Production distribution in cellulose hydrolysis with varying carbon treatment times. Carbon treatment times: 10, 20, and 45 min; hydrolysis conditions: 150 °C for 24 h. Glucose yield and cellulose conversion using the original carbon catalyst are 1.3% and 6.3%, respectively; CNTs treated by negative plasma achieved 34.6% cellulose conversion and 22.5% glucose yield.

hydrolysis achieved a glucose yield of 62.90% with a cellobiose conversion of 70%, outperforming many previously reported carbon-based solid acid catalysts under comparable reaction conditions [11]. In comparison, heat-activation treated CNTs further increased the glucose yield to 72% while simultaneously suppressing the formation of undesired byproducts, indicating a more selective hydrolysis pathway.

4. Conclusions

This study elucidates the reaction mechanisms underlying plasma-driven carbon sulfonation and demonstrates its potential as an environmentally benign and efficient strategy for carbon functionalization. Plasma discharge in dilute sulfuric acid generates $\bullet SO_4^-$ in the liquid phase, enabling the incorporation of–SO_3H, –OSO_3H, and other oxygen-containing functional groups onto carbon surfaces. The formation of $\bullet SO_4^-$ is primarily attributed to the rapid reaction between plasma-generated •OH and HSO_4^- ions at the plasma–liquid interface. By combining plasma treatment with UV- and heat-activated $Na_2S_2O_8$ reference systems, this work establishes a mechanistic framework that clarifies the role of $\bullet SO_4^-$ in carbon sulfonation while highlighting the contributions of plasma-specific effects, such as localized radical generation and surface activation. These insights provide a fundamental basis for rational optimization of plasma sulfonation processes. In addition, the DC plasma-treated CNTs exhibited a 34.6% cellulose conversion and 22.5% glucose yield during cellulose hydrolysis, a glucose yield of 62.90%, and a cellobiose conversion rate of 70% during cellobiose hydrolysis. These findings support the development of more efficient and sustainable methods for producing sulfonated carbon catalysts via plasma treatment, broadening their applications across various catalytic and industrial processes.

CRediT authorship contribution statement

Siqi Deng: Writing – original draft, Methodology, Investigation, Formal analysis, Data curation, Conceptualization. **Kaixun Yao:** Writing – review & editing, Formal analysis, Data curation. **Manabu Kodama:** Writing – review & editing, Formal analysis, Data curation. **Katsuyuki Takahashi:** Writing – review & editing, Formal analysis, Data curation. **Kosuke Tachibana:** Writing – review & editing, Formal analysis, Data curation. **Junko Hieda:** Writing – review & editing, Formal analysis, Data curation. **Oi Lun Li:** Writing – review & editing, Formal analysis, Data curation. **Nozomi Takeuchi:** Writing – review & editing,

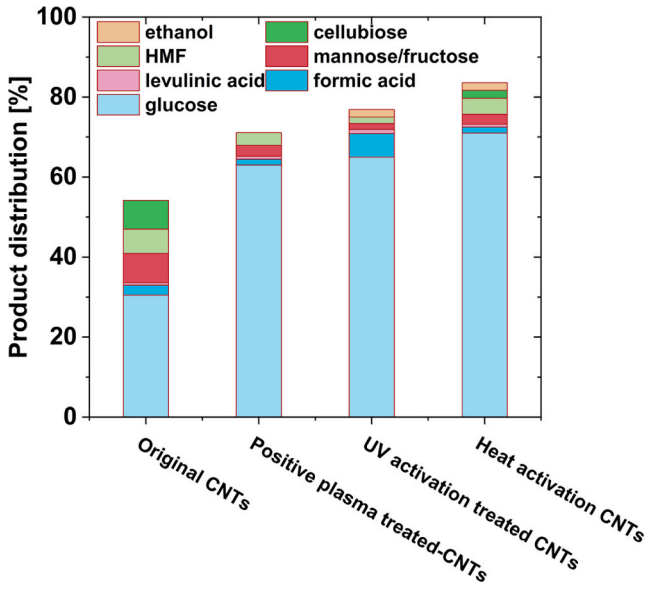

Fig. 10. Production distribution in cellobiose hydrolysis with three kinds of treated CNTs (45 min Positive plasma treatment, 45 min UV-activation treatment and 45 min heat activation treatment). Hydrolysis temperature: 150 °C; hydrolysis time: 24 h.

Supervision, Project administration, Formal analysis, Data curation.

Declaration of competing interest

The authors declare that they have no known competing financial interests or personal relationships that could have appeared to influence the work reported in this paper.

Acknowledgments

This work was partially supported by Japan Power Academy, Environment Research and Technology Development Fund of the Environmental Restoration (JPMEERF20223R01) and JST SPRING, Japan (JPMJSP2106 and JPMJSP2180). The authors thank the Tokyo Tech Academy of Energy and Informatics (ISE) for financial assistance. The authors would like to express their gratitude to the Materials Analysis Division, Open Facility Center at the Science Tokyo, for their support with the CHNS and TEM analyses. In addition, they extend their gratitude to the Materials Advanced Research Infrastructure (ARIM) at the University of Tokyo for providing access to their XPS equipment.

Appendix A. Supplementary material

Supplementary data to this article can be found online at https://doi.org/10.1016/j.apsusc.2026.167120.

Data availability

Data will be made available on request.

References

[1] D. Rivin, J. Aron, L.B. Richards, Sulfonated carbon blacks, US3442679A, 1969. https://patents.google.com/patent/US3442679A/en (accessed September 4, 2025).
[2] S. Suganuma, K. Nakajima, M. Kitano, D. Yamaguchi, H. Kato, S. Hayashi, M. Hara, Hydrolysis of cellulose by amorphous carbon bearing SO3H, COOH, and OH groups, J. Am. Chem. Soc. 130 (2008) 12787–12793, https://doi.org/10.1021/ja803983h.
[3] M. Toda, A. Takagaki, M. Okamura, J.N. Kondo, S. Hayashi, K. Domen, M. Hara, Biodiesel made with sugar catalyst, Nature 438 (2005) 178, https://doi.org/10.1038/438178a.
[4] M. Hara, T. Yoshida, A. Takagaki, T. Takata, J.N. Kondo, S. Hayashi, K. Domen, A carbon material as a strong protonic acid, Angew. Chem. Int. Ed. 43 (2004) 2955–2958, https://doi.org/10.1002/anie.200453947.
[5] L.J. Konwar, P. Mäki-Arvela, J.-P. Mikkola, SO_3H-containing functional carbon materials: synthesis, structure, and acid catalysis, Chem. Rev. 119 (2019) 11576–11630, https://doi.org/10.1021/acs.chemrev.9b00199.
[6] S. Suganuma, K. Nakajima, M. Kitano, H. Kato, A. Tamura, H. Kondo, S. Yanagawa, S. Hayashi, M. Hara, SO_3H-bearing mesoporous carbon with highly selective catalysis, Microporous Mesoporous Mater. 143 (2011) 443–450, https://doi.org/10.1016/j.micromeso.2011.03.028.
[7] J. Ji, G. Zhang, H. Chen, S. Wang, G. Zhang, F. Zhang, X. Fan, Sulfonated graphene as water-tolerant solid acid catalyst, Chem. Sci. 2 (2011) 484–487, https://doi.org/10.1039/C0SC00484G.
[8] Q. Guan, Y. Li, Y. Chen, Y. Shi, J. Gu, B. Li, R. Miao, Q. Chen, P. Ning, Sulfonated multi-walled carbon nanotubes for biodiesel production through triglycerides transesterification, RSC Adv. 7 (2017) 7250–7258, https://doi.org/10.1039/C6RA28067F.
[9] O.L. Li, L. Qin, N. Takeuchi, K. Kim, T. Ishizaki, Effect of hydrophilic/hydrophobic properties of carbon materials on plasma-sulfonation process and their catalytic activities in cellulose conversion, Catal. Today 337 (2019) 155–161, https://doi.org/10.1016/j.cattod.2019.04.025.
[10] O.L. Li, R. Ikura, T. Ishizaki, Hydrolysis of cellulose to glucose over carbon catalysts sulfonated via a plasma process in dilute acids, Green Chem. 19 (2017) 4774–4777, https://doi.org/10.1039/C7GC02143G.
[11] L. Qin, N. Takeuchi, K. Takahashi, J. Kang, K.H. Kim, O.L. Li, N2/Ar plasma-induced surface sulfonation on graphene nanoplatelets for catalytic hydrolysis of cellulose to glucose, Appl. Surf. Sci. 545 (2021) 149051, https://doi.org/10.1016/j.apsusc.2021.149051.
[12] L. Qin, T. Ishizaki, N. Takeuchi, K. Takahashi, K.H. Kim, O.L. Li, Green sulfonation of carbon catalysts via gas–liquid interfacial plasma for cellulose hydrolysis, ACS Sustain. Chem. Eng. 8 (2020) 5837–5846, https://doi.org/10.1021/acssuschemeng.9b07156.
[13] Q. Chen, J. Li, Y. Li, A review of plasma–liquid interactions for nanomaterial synthesis, J. Phys. D Appl. Phys. 48 (2015) 424005, https://doi.org/10.1088/0022-3727/48/42/424005.
[14] L. Di, J. Zhang, X. Zhang, H. Wang, H. Li, Y. Li, D. Bu, Cold plasma treatment of catalytic materials: a review, J. Phys. D Appl. Phys. 54 (2021) 333001, https://doi.org/10.1088/1361-6463/ac0269.
[15] T.I.T. Okpalugo, P. Papakonstantinou, H. Murphy, J. Mclaughlin, N.M.D. Brown, Oxidative functionalization of carbon nanotubes in atmospheric pressure filamentary dielectric barrier discharge (APDBD), Carbon 43 (2005) 2951–2959, https://doi.org/10.1016/j.carbon.2005.06.033.
[16] Z. Zhang, J.L. Wilson, B.R. Kitt, D.W. Flaherty, Effects of oxygen plasma treatments on surface functional groups and shear strength of carbon fiber composites, ACS Appl. Polym. Mater. 3 (2021) 986–995, https://doi.org/10.1021/acsapm.0c01270.
[17] S. Hoshino, K. Kawahara, N. Takeuchi, Hydrophilization of graphite using plasma above/in a solution, Jpn. J. Appl. Phys. 57 (2017) 0102B1, https://doi.org/10.7567/JJAP.57.0102B1.
[18] G.V. Buxton, C.L. Greenstock, W.P. Helman, A.B. Ross, Critical Review of rate constants for reactions of hydrated electrons, hydrogen atoms and hydroxyl radicals (·OH/·O− in Aqueous solution, J. Phys. Chem. Ref. Data 17 (1988) 513–886, https://doi.org/10.1063/1.555805.
[19] X. Zhang, L. Lei, B. Xia, Y. Zhang, J. Fu, Oxidization of carbon nanotubes through hydroxyl radical induced by pulsed O_2 plasma and its application for O_2 reduction in electro-Fenton, Electrochim. Acta 54 (2009) 2810–2817, https://doi.org/10.1016/j.electacta.2008.11.029.
[20] S. Yonemori, R. Ono, Flux of OH and O radicals onto a surface by an atmospheric-pressure helium plasma jet measured by laser-induced fluorescence, J. Phys. D Appl. Phys. 47 (2014) 125401, https://doi.org/10.1088/0022-3727/47/12/125401.
[21] X.Y. Liu, X.K. Pei, K. Ostrikov, X.P. Lu, D.W. Liu, The production mechanisms of OH radicals in a pulsed direct current plasma jet, Phys. Plasmas 21 (2014) 093513, https://doi.org/10.1063/1.4895496.
[22] H. Ishigame, S. Nishiyama, K. Sasaki, Spatial distribution of OH radical density in atmospheric-pressure dc helium glow plasma in contact with electrolyte solution, Jpn. J. Appl. Phys. 54 (2014) 01AF02, https://doi.org/10.7567/JJAP.54.01AF02.
[23] A.F.F. da Silva, N.A. Debacher, C.P. Gretter, L.O.B. Benetoli, A simple and low-cost method of sulfur functionalization and aqueous dispersion of graphene driven by gas-liquid non-thermal plasma discharge, Carbon Trends 12 (2023) 100289, https://doi.org/10.1016/j.cartre.2023.100289.
[24] S. Deng, N. Takeuchi, J. Hieda, K. Takahashi, K. Tachibana, O.L. Li, Investigation of the sulfonation mechanism by gas–liquid interfacial plasma under atmospheric pressure conditions, J. Phys. D Appl. Phys. 55 (2022) 345205, https://doi.org/10.1088/1361-6463/ac73c2.
[25] P.-Y. Jiang, Y. Katsumura, R. Nagaishi, M. Domae, K. Ishikawa, K. Ishigure, Y. Yoshida, Pulse radiolysis study of concentrated sulfuric acid solutions. Formation mechanism, yield and reactivity of sulfate radicals, J. Chem. Soc. Faraday Trans. 88 (1992) 1653–1658, https://doi.org/10.1039/FT9928801653.
[26] S.B. Hammouda, F. Zhao, Z. Safaei, D.L. Ramasamy, B. Doshi, M. Sillanpää, Sulfate radical-mediated degradation and mineralization of bisphenol F in neutral medium by the novel magnetic Sr_2CoFeO_6 double perovskite oxide catalyzed peroxymonosulfate: influence of co-existing chemicals and UV irradiation, Appl. Catal. B 233 (2018) 99–111, https://doi.org/10.1016/j.apcatb.2018.03.088.
[27] X. Duan, X. Niu, J. Gao, S. Wacławek, L. Tang, D.D. Dionysiou, Comparison of sulfate radical with other reactive species, Curr. Opin. Chem. Eng. 38 (2022) 100867, https://doi.org/10.1016/j.coche.2022.100867.

[28] O.S. Furman, A.L. Teel, R.J. Watts, Mechanism of base activation of persulfate, Environ. Sci. Technol. 44 (2010) 6423–6428, https://doi.org/10.1021/es1013714.

[29] G. Ran, Q. Li, Degradation of refractory organic compounds from dinitrodiazophenol containing industrial wastewater through UV/H_2O_2 and UV/PS processes, Environ. Sci. Pollut. Res. 27 (2020) 6042–6051, https://doi.org/10.1007/s11356-019-07367-1.

[30] I. Rivas-Zaballos, L. Romero-Martínez, I. Moreno-Garrido, J. Moreno-Andrés, A. Acevedo-Merino, E. Nebot, UV-LEDs combined with persulfate salts as a method to inactivate microalgae in ballast water, J. Water Process Eng. 51 (2023) 103361, https://doi.org/10.1016/j.jwpe.2022.103361.

[31] C.-M. Hung, C.-W. Chen, Y.-Y. Liu, C.-D. Dong, Decolorization of methylene blue by persulfate activated with FeO magnetic particles, Water Environ. Res 88 (2016) 675–686.

[32] Y. Liu, L. Liu, Y. Wang, A critical review on removal of gaseous pollutants using sulfate radical-based advanced oxidation technologies, Environ. Sci. Technol. 55 (2021) 9691–9710, https://doi.org/10.1021/acs.est.1c01531.

[33] J. Wang, S. Wang, Activation of persulfate (PS) and peroxymonosulfate (PMS) and application for the degradation of emerging contaminants, Chem. Eng. J. 334 (2018) 1502–1517, https://doi.org/10.1016/j.cej.2017.11.059.

[34] S. Wacławek, H.V. Lutze, K. Grübel, V.V.T. Padil, M. Černík, D. Dionysios Dionysiou, Chemistry of persulfates in water and wastewater treatment: a review, Chem. Eng. J. 330 (2017) 44–62, https://doi.org/10.1016/j.cej.2017.07.132.

[35] P. Bruggeman, C. Leys, Non-thermal plasmas in and in contact with liquids, J. Phys. D Appl. Phys. 42 (2009) 053001, https://doi.org/10.1088/0022-3727/42/5/053001.

[36] L.R. Ventura, C.E. Fellows, The N2 second positive (C3Πu→B3Πg) system reviewed: improved data and analysis, J. Quant. Spectrosc. Radiat. Transf. 239 (2019) 106645, https://doi.org/10.1016/j.jqsrt.2019.106645.

[37] H.I.A. Qazi, Q.-Y. Nie, H.-P. Li, X.-F. Zhang, C.-Y. Bao, Comparison of electrical and optical characteristics in gas-phase and gas-liquid phase discharges, Phys. Plasmas 22 (2015) 123512, https://doi.org/10.1063/1.4937779.

[38] P. Bruggeman, D.C. Schram, M.G. Kong, C. Leys, Is the rotational temperature of OH(A–X) for discharges in and in contact with liquids a good diagnostic for determining the gas temperature? Plasma Processes Polym. 6 (2009) 751–762, https://doi.org/10.1002/ppap.200950014.

[39] X. Chen, X. Wang, D. Fang, A review on C1s XPS-spectra for some kinds of carbon materials, Fullerenes, Nanotubes, Carbon Nanostruct. 28 (2020) 1048–1058, https://doi.org/10.1080/1536383X.2020.1794851.

[40] M.C. Biesinger, Accessing the robustness of adventitious carbon for charge referencing (correction) purposes in XPS analysis: Insights from a multi-user facility data review, Appl. Surf. Sci. 597 (2022) 153681, https://doi.org/10.1016/j.apsusc.2022.153681.

[41] D.J. Miller, M.C. Biesinger, N.S. McIntyre, Interactions of CO_2 and CO at fractional atmosphere pressures with iron and iron oxide surfaces: one possible mechanism for surface contamination? Surf. Interface Anal. 33 (2002) 299–305, https://doi.org/10.1002/sia.1188.

[42] L.H. Grey, H.-Y. Nie, M.C. Biesinger, Defining the nature of adventitious carbon and improving its merit as a charge correction reference for XPS, Appl. Surf. Sci. 653 (2024) 159319, https://doi.org/10.1016/j.apsusc.2024.159319.

[43] S. Deng, N. Takeuchi, T. Kaneko, Atmospheric pressure plasma for carbon material modification and synthesis: a comprehensive review, Materials 18 (2025) 5662, https://doi.org/10.3390/ma18245662.

[44] T.T. Vi Tran, S. Kongparakul, P. Reubroycharoen, G. Guan, M.H. Nguyen, N. Chanlek, C. Samart, Production of furan based biofuel with an environmental benign carbon catalyst, Environ. Prog. Sustain. Energy 37 (2018) 1455–1461, https://doi.org/10.1002/ep.12796.

[45] U.I. Nda-Umar, I. Ramli, E.N. Muhamad, Y.H. Taufiq-Yap, N. Azri, Synthesis and characterization of sulfonated carbon catalysts derived from biomass waste and its evaluation in glycerol acetylation, Biomass Conv. Bioref. 12 (2022) 2045–2060, https://doi.org/10.1007/s13399-020-00784-0.

[46] X. Li, Y. Wang, X. Xie, C. Huang, S. Yang, Dehydration of fructose, sucrose and inulin to 5-hydroxymethylfurfural over yeast-derived carbonaceous microspheres at low temperatures, RSC Adv. 9 (2019) 9041–9048, https://doi.org/10.1039/C8RA10465D.

[47] T. Tromm Steffen, L. César Fontana, P. Hammer, D. Becker, Amine functionalization of carbon nanotubes with solid urea using different plasma treatments, Appl. Surf. Sci. 583 (2022) 152493, https://doi.org/10.1016/j.apsusc.2022.152493.

[48] Microwave-assisted biodiesel production using –SO3H functionalized heterogeneous catalyst derived from a lignin-rich biomass | Scientific Reports, (n.d.). https://www.nature.com/articles/s41598-023-36380-1 (accessed October 26, 2025).

[49] Y. Cai, X. Zhao, Y. Wang, D. Ma, S. Xu, Enhanced desalination performance utilizing sulfonated carbon nanotube in the flow-electrode capacitive deionization process, Sep. Purif. Technol. 237 (2020) 116381, https://doi.org/10.1016/j.seppur.2019.116381.

[50] L.T. Weng, P. Bertrand, J.H. Stone-Masui, W.E.E. Stone, Desorption of emulsifiers from polystyrene latexes studied by various surface techniques: a comparison between XPS, ISS, and static SIMS, Langmuir 13 (1997) 2943–2952, https://doi.org/10.1021/la962078s.

[51] K.A. Wepasnick, B.A. Smith, J.L. Bitter, D. Howard Fairbrother, Chemical and structural characterization of carbon nanotube surfaces, Anal. Bioanal. Chem. 396 (2010) 1003–1014, https://doi.org/10.1007/s00216-009-3332-5.

[52] Crystalline Ropes of Metallic Carbon Nanotubes | Science, (n.d.). https://www.science.org/doi/10.1126/science.273.5274.483 (accessed January 26, 2026).

[53] M.S. Dresselhaus, G. Dresselhaus, P. Avouris, in: Carbon Nanotubes, Springer, Berlin, Heidelberg, 2001, https://doi.org/10.1007/3-540-39947-X.

[54] A. Jorio, R. Saito, Raman spectroscopy for carbon nanotube applications, J. Appl. Phys. 129 (2021) 021102, https://doi.org/10.1063/5.0030809.

[55] M.S. Dresselhaus, G. Dresselhaus, R. Saito, A. Jorio, Raman spectroscopy of carbon nanotubes, Phys. Rep. 409 (2005) 47–99, https://doi.org/10.1016/j.physrep.2004.10.006.

[56] M.M. Ngoma, M. Mathaba, K. Moothi, Effect of carbon nanotubes loading and pressure on the performance of a polyethersulfone (PES)/carbon nanotubes (CNT) membrane, Sci. Rep. 11 (2021) 23805, https://doi.org/10.1038/s41598-021-03042-z.

[57] N.O. Ramoraswi, P.G. Ndungu, Photo-catalytic properties of TiO_2 supported on MWCNTs, SBA-15 and silica-coated MWCNTs nanocomposites, Nanoscale Res. Lett. 10 (2015) 427, https://doi.org/10.1186/s11671-015-1137-3.

[58] Y.-C. Chiang, W.-H. Lin, Y.-C. Chang, The influence of treatment duration on multi-walled carbon nanotubes functionalized by H_2SO_4/HNO_3 oxidation, Appl. Surf. Sci. 257 (2011) 2401–2410, https://doi.org/10.1016/j.apsusc.2010.09.110.

[59] M.A. Atieh, Removal of Chromium (VI) from polluted water using carbon nanotubes supported with activated carbon, Procedia Environ. Sci. 4 (2011) 281–293, https://doi.org/10.1016/j.proenv.2011.03.033.

[60] S. Costa, E. Borowiak-Palen, M. Kruszyńska, A. Bachmatiuk, R.J. Kaleńczuk, Characterization of carbon nanotubes by Raman spectroscopy, (n.d.).

[61] S.L.H. Rebelo, A. Guedes, M.E. Szefczyk, A.M. Pereira, J.P. Araújo, C. Freire, in: Progress in the Raman Spectra Analysis of Covalently Functionalized Multiwalled Carbon Nanotubes: Unraveling Disorder in Graphitic Materials, 2016, https://doi.org/10.1039/C5CP06519D.

[62] Z.-M. Lin, P.-C. Huang, L.-K. Chu, Reaction kinetics of the sulfate radical (SO4–) upon ultraviolet photolysis of persulfate (S2O82−) aqueous solution, Chem. Phys. Lett. 849 (2024) 141415, https://doi.org/10.1016/j.cplett.2024.141415.

[63] K.E. Manz, I. Kulaots, C.A. Greenley, P.J. Landry, K.V. Lakshmi, M.J. Woodcock, L. Hellerich, J.D. Bryant, M. Apfelbaum, K.D. Pennell, Low-temperature persulfate activation by powdered activated carbon for simultaneous destruction of perfluorinated carboxylic acids and 1,4-dioxane, J. Hazard. Mater. 442 (2023) 129966, https://doi.org/10.1016/j.jhazmat.2022.129966.

[64] N. Zrinyi, A.-L.-T. Pham, Oxidation of benzoic acid by heat-activated persulfate: effect of temperature on transformation pathway and product distribution, Water Res. 120 (2017) 43–51, https://doi.org/10.1016/j.watres.2017.04.066.

[65] Z. Xia, Z. Ye, T. Deng, Z. Tan, C. Song, J. Li, Benzylic C−H radical sulfation by persulfates, Angew. Chem. Int. Ed. 64 (2025) e202413847, https://doi.org/10.1002/anie.202413847.

[66] G. Moad, D.H. Solomon, 8 - Azo and Peroxy Initiators, in: G. Allen, J.C. Bevington (Eds.), Comprehensive Polymer Science and Supplements, Pergamon, Amsterdam, 1989: pp. 97–121. Doi: 10.1016/B978-0-08-096701-1.00070-7.

[67] T. Li, S. Lu, W. Lin, H. Ren, R. Zhou, Heat-activated persulfate oxidative degradation of ofloxacin: kinetics, mechanisms, and toxicity assessment, Chem. Eng. J. 433 (2022) 133801, https://doi.org/10.1016/j.cej.2021.133801.

[68] Aromatic sulfonation, Wikipedia (2024). https://en.wikipedia.org/w/index.php?title=Aromatic_sulfonation&oldid=1262982889 (accessed December 15, 2024).

[69] Y. Yue, S. Exarhos, J. Nam, D. Lee, S. Linic, P.J. Bruggeman, Quantification of plasma produced OH and electron fluxes at the liquid anode and their role in plasma driven solution electrochemistry, Plasma Sources Sci. Technol. 31 (2022) 125008, https://doi.org/10.1088/1361-6595/acab29.

[70] Y. Chen, C. Feng, C. Jin, Y. Zhu, J. Huang, H. Na, J. Zhu, In situ bifunctional solid acids bearing B–OH and –COOH groups for efficient hydrolysis of cellulose to sugar in a pure aqueous phase, Green Chem. 26 (2024) 948–959, https://doi.org/10.1039/D3GC04100J.

[71] M. Kitano, D. Yamaguchi, S. Suganuma, K. Nakajima, H. Kato, S. Hayashi, M. Hara, Adsorption-enhanced hydrolysis of β-1,4-glucan on graphene-based amorphous carbon bearing SO_3H, COOH, and OH groups, Langmuir 25 (2009) 5068–5075, https://doi.org/10.1021/la8040506.